Czech Technical University in Prague
Faculty of Nuclear Sciences and Physical Engineering
Department of Physical Electronics

Laser-Plasma Interaction in the Inertial Fusion Context

(Research project)

Author: Bc. Petr Valenta
Supervisor: doc. Ing. Ondřej Klimo, Ph.D.
Consultants: prof. Ing. Jiří Limpouch, CSc.
Dr. Stefan Weber
Academic year: 2015/2016

Declaration

I declare that I carried out this work independently, and only with the cited sources, literature and other professional sources.

In Prague on .....

.....
Bc. Petr Valenta

Contents

Introduction

Despite a wide variety of economic drives, the world energy consumption is continuously growing. Fossil fuels, crude oil and natural gas reserves are slowly shrinking and renewable resources alone will definitely not be able to meet the global energy demand. This energetic deficit might become a serious obstacle in the further sustainable development of human society. Therefore it is essential to find an alternative energy source; preferably one which could finally solve all of the aforementioned problems and, in addition, its utilization would be environmentally friendly.

During the 1950s, the demand for alternative and more feasible energy sources for the near future has led to the intensive research in the field of nuclear power engineering. Particularly, scientists became interested in a peaceful use of thermonuclear fusion. Firstly, they have tried to make required conditions for the fusion plasma using convenient geometry of magnetic fields. Early success, which has been expected by the scientific community, however, has not been achieved. Several years later, this fact also contributed to the idea of using lasers, at that time an entirely new source of intense radiation, to ignite thermonuclear fusion. It soon turned out, however, that by using lasers, a wide range of phenomena which might seriously complicate the ignition is inevitable as well.

One of the most negative effects in terms of inertial confinement fusion is the generation of hot electrons in a coronal plasma, in which the laser energy is transmitted to the kinetic energy of plasma. These electrons significantly preheat the core of the fuel target, which makes the required compression of plasma more difficult. Therefore, the laser-plasma interactions in this context have been intensively studied [27]. At the same time, new, more sophisticated methods, whereby laser energy is deposited into the target as efficiently as possible and with a minimal production of hot electrons, have been investigated as well [4].

The following work is focused on the interaction of laser radiation with plasma for the conditions according to current experiments in the Prague Asterix Laser System (PALS) facility, where the possibilities of fuel ignition are studied using a high-power iodine laser. More specifically, the interaction in terms of laser energy absorption efficiency, hot electron production and laser light scattering in a regime relevant to the shock ignition scheme, which has been proposed recently [5], have all been studied.

The work is structured as follows: the first chapter provides a brief description of the thermonuclear fusion, including the conditions of its ignition for both basic approaches.

The major part is devoted to inertial fusion. The second chapter summarizes the elementary knowledge of plasma physics and physics of laser-plasma interaction. The third chapter describes numerical simulation as an essential tool in modern science and engineering. Especially, one of the most popular methods in plasma physics, particle-in-cell (PIC), is thoroughly discussed. The characteristics of the code EPOCH[1], which has been used for the simulations within this work, can be found in the last section of this chapter. The last chapter demonstrates the results and benefits of this work. It contains the implementation of the boundary conditions in the code EPOCH and the results of performed two-dimensional simulations.

Although the most convenient unit system for most plasma applications is the Gaussian cgs system, throughout this work the SI (System Internationale) units are used, unless explicitly stated.

Chapter 1

Inertial fusion

The energy contained in an atomic nucleus can be obtained in two different ways. The first one consists in the splitting of heavy atomic nuclei into lighter elements. However, fission reaction entails some safety risks. In addition, the products of this reaction themselves are often unstable, and therefore give off relatively large amounts of radiation which cause some serious difficulties with their long term storage.

The second approach is nuclear fusion. It is the exact opposite process in which two or more atomic nuclei come very close and then join together to form a new type of atomic nucleus. If the mass of the product is less than the sum of the masses of the initial fusing nuclei, an amount of energy corresponding to this mass deficit is released in accordance with Einstein's famous relation. This chapter provides a brief insight into the challenges of nuclear fusion, particularly to one of the main approaches to achieve it - inertial confinement fusion.

1.1 Principles of nuclear fusion

In order to achieve fusion, the reacting nuclei have to get very close to each other to activate the strong nuclear force. However, there is a large electrostatic repulsion between them as they come together because the protons in nuclei are positively charged. There are several possibilities of overcoming this barrier. One can for example utilize the initial kinetic energy of the chaotic thermal motion of the particles. In thermal equilibrium, the Coulomb collisions redistribute the kinetic energy among the plasma particles, and fusion reactions will eventually occur after a sequence of collisions. This approach is called thermonuclear fusion.

Reactions which could be usable in the case of the energy production on Earth must have high cross-section values at relatively low required incident energies. Furthermore, the economic viability and competitiveness is crucial for commercial use of fusion power. In other words, the reaction must be able to cover obviously no less than the energetic costs incurred for its ignition. The word ignition refers to the moment when a controlled fusion reaction generates as much or more energy than is needed to spark the reaction. In regards to each

of these attributes, the best reaction candidate appears to be the reaction of two hydrogen isotopes - deuterium and tritium,

$$^{2}_{1}\mathrm{H} + ^{3}_{1}\mathrm{H} \rightarrow ^{4}_{2}\mathrm{He}\ (3{,}5\ \mathrm{MeV}) + ^{1}_{0}\mathrm{n}\ (14{,}1\ \mathrm{MeV}). \tag{1.1}$$

Deuterium has quite rich natural abundance in Earth's oceans, thus it is commonly available in sufficient quantity. The efficient extraction from seawater is supposed to be technically ready [7]. On the contrary, naturally occurring tritium is extremely rare due to its short half-life, therefore the fuel cycle requires the breeding of tritium. The production is possible with irradiation of lithium by fusion neutrons using the following reaction,

$$^{6}_{3}\mathrm{Li} + ^{1}_{0}\mathrm{n} \rightarrow ^{4}_{2}\mathrm{He}\ (2{,}1\ \mathrm{MeV}) + ^{3}_{1}\mathrm{H}\ (2{,}7\ \mathrm{MeV}). \tag{1.2}$$

Lithium is widely distributed in the Earth's crust and seawater. Consequently, both fusion fuel resources are relatively easily accessible, uniformly geographically distributed and have near unlimited availability. The product of their reaction is a neutron and a helium nucleus, of which the latter product is not radioactive. These attributes and the potential to produce large amounts of carbon-free energy with almost no environmental impact predetermine nuclear fusion to become a global energy source.

1.2 Lawson criterion

The first attempts to make the fusion reaction in terrestrial conditions are heading into the 1930s. The idea was to collide deuteron beams with heavy water vapor using a particle accelerator. This approach is referred to as beam fusion [22]. The resulting reaction led to the release of a large number of particles including among other a helium nuclei. However, it was soon revealed that this would not be a feasible way for power production. Even though the process also releases heat, much more energy is consumed for accelerating the particles. The deuteron beams lose their energy by the ionization or elastic Coulomb collisions with target nuclides whose cross-section is several orders of magnitude higher. Thus the probability of nuclear fusion is almost negligible.

After the worldwide declassification of fusion research in 1956, J. D. Lawson submitted his article for publication [19]. In it, the conditions that have to be fulfilled in order to reach ignition in thermonuclear reactor were demonstrated. As originally formulated, the Lawson criterion gives a minimum required value for the product of the plasma density and the confinement time. This value depends on the plasma temperature which has to be significantly high for all kinds of reactants. It is obvious, since the involved particles have to acquire sufficient kinetic energy to overcome electric repulsion, as mentioned before, and thus increase the rate of fusion reactions.

Even though the Coulomb barrier is penetrated by quantum tunneling, allowing the process to proceed at lower temperatures, the vast majority of substances are in the state

of a fully or partially ionized plasma under that conditions. However, exposing any solid material to hot plasmas can damage the material, which then emit impurities contaminating the plasma and decreasing its temperature and confinement stability. Hence, the fundamental question is how to confine such a fusion plasma in the terrestrial conditions.

Taking into account that plasma consists of charged particles, one can exploit a magnetic field of appropriate geometry to shape and confine them. The charged particles will then follow helical paths encircling the magnetic lines of force. However, the intensity of the magnetic field is limited by the structural characteristics of matter, thus it is possible to confine only low density plasmas. From Lawson's criterion, one can clearly find out that in this case fusion reactions have to take place for a relatively long time period.

The second route to confine hot plasmas is to take advantage of the inertia of the mass itself. The fusion burn can occur before the plasma escapes into the surrounding environment. Mass inertia keeps it together for a certain moment given by the time depending on the velocity of an acoustic wave, thus it involves no external means of confinement. The confinement time is obviously very short in this approach, therefore it is necessary to compress the solid fuel to extremely high densities.

1.3 Direct and indirect drive

The release of the nuclear energy by the inertial confinement fusion was demonstrated for the first time using a thermonuclear bomb shortly after the World War II. The devastating effects of explosion are, however, indisputable in that range. It is desirable to obtain the energy in a controlled and meaningful manner. These considerations lead to a typical values of the fusion energy which can be produced by burning only a few milligrams of a deuterium and tritium mixture. In a cryogenic state, such amount of the fuel fits into the volume of a sphere with a diameter of one millimeter. There appeared, however, to be no source powerful enough to deposit sufficient amount of energy into such a small area to induce thermonuclear fusion. Therefore, the inertial confinement was no further taken into account.

Things have changed when the first working laser was demonstrated by T. H. Maiman in the beginning of the 1960s. The idea of achieving nuclear fusion by laser irradiation is based on the conservation of momentum. Multiple intensive beams of laser pulses can be focused directly on a small spherical capsule containing mixture of nuclear fuel. The beam energy deposition leads to the rapid heating and ablation of the outer surface of the capsule shell, forming a coronal plasma that expands into a surrounding vacuum. This process generates a high pressure which accelerates the inner part of the shell inwards. Then the enormous implosion is driven via the rocket effect. It should be understood that it is not beam pressure acting on the target surface, but the ablation pressure generated by the recoil of the expanding material. Under certain conditions, it is possible to achieve the required level of compression for the ignition of the nuclear fuel. This scheme is known as direct drive [3].

However, the direct drive entails some serious physics issues and constraints. Primarily, the target implosion is inherently susceptible to hydrodynamic instabilities that lead immediately to the ignition failure. These arise by the very small irradiation non-uniformities due to the finite number of naturally coherent driver beams and due to the macroscopic imperfections on the target surface. In addition, the interaction of high-power laser beams with coronal plasma can generate the population of hot electrons. These subsequently move towards the target core causing premature excessive fuel preheat that makes the compression more difficult. Ideally, the core of the capsule should reach the ignition temperature at the time of the maximum compression to achieve a minimum cost of driver energy [2].

To minimize the growth of the instabilities, it was later proposed to insert the fusion fuel capsule into a cylindrical cavity made of a largely opaque material. This cavity is today known as a hohlraum [21]. The laser beams are pointed through holes onto the interior surface of the hohlraum, which in turn absorbs and emits approximately black body radiation in the form of X-rays. The significant advantage with this approach is that the energy is re-radiated in a much more symmetric fashion than would be possible in the direct drive approach, resulting in a more uniform implosion. This configuration, which is very similar to the original hydrogen bomb design, is known as indirect drive [2].

The downside to using this approach is obviously lower overall efficiency of energy transfer. The partial loss of the radiation source energy takes place during conversion into thermal X-rays, another significant radiation loss occurs mainly through the beam entrance windows of the hohlraum to the outside. Consequently, only a small fraction of laser energy is absorbed by the capsule.

In addition, the laser intensity in the plasma corona is above the threshold that gives rise to parametric instabilities, mainly stimulated Raman scattering, Brillouin scattering and two-plasmon decay. The study of these parametric instabilities and the interplay between them is provided in the second chapter of this work.

1.4 Modern approaches

The intensive research and development in the field of laser technology have seen a tremendous progress over the last five decades. New technologies has improved the quality of lasers and offered the prospect of building ultra-short pulsed laser facilities of an extremely high peak output power. Thanks to that, this source of coherent light allows many experiments in various fields of human research to be performed, which otherwise would not be possible. Laser is a unique device that provides an unprecedented capability for the laboratory study of a matter at high energy densities, its interaction with intense radiation and for meeting the challenge of controlled thermonuclear fusion. Therefore, it is no coincidence that a new, more sophisticated methods and techniques of its ignition have been discovered recently.

In the early days of the fusion research, it was thought that the whole volume of the fuel has to be heated and compressed to the fusion conditions. It soon turned out, however, that

this would require an unrealistically high amount of driver energy. The solution could be the ignition only of a small fraction of the fuel assembly [24]. At the moment of stagnation, the plasma at the center of the fuel reaches the highest pressure and temperature as the result of a spherical implosion. If the drive symmetry requirements are achieved, the fusion reactions should start in this region. Once the core of the capsule starts to burn, the energy produced by the fusion reactions is sufficient to heat up the rest of the capsule. A thermonuclear burn wave is then spreading outwards, igniting the whole fuel, which expands rapidly. In this approach, the cold fuel is compressed at minimum energy, and the total energy to be invested into the fuel is therefore significantly reduced. This is known as a central hot-spot ignition scenario [25].

Although the hot-spot approach has a potential for a success, there is also considerable interest in a complementary scheme called fast ignition [2], in which compression phase is separated from the ignition. In this concept, a target is compressed without the requirement to form the central hot-spot, thus it relaxes symmetry requirements significantly. The hot-spot will be then located asymmetrically at the periphery of the compressed fuel core, since the idea is to provide the ignition by an external trigger, which could be an additional high-energy laser pulse.

The crucial question for this concept is how to efficiently transport such a pulse into a dense plasma. The problem is that the compressed plasma is surrounded by an extended corona which is prone to parametric instabilities. One way to bring the laser beam closer to the fuel core is offered by the intense laser beam itself, which tends to bore a hole into the overdense plasma. Another straightforward experimental approach is to guide the beam by a gold cone.

A third, relatively new scenario, which is called shock ignition, might also offer another route to achieving ignition in a non-isobaric target. The cryogenic shell is initially imploded at low velocity using a laser drive of modest peak power and low total energy. The assembled fuel is then separately ignited from a central hotspot heated by a strong, spherically convergent shock wave driven by a high intensity spike at the end of the laser pulse. The launching of the ignition shock is timed to reach the center just as the main fuel is stagnating and starting to rebound [26].

As it involves low velocity implosions, this scheme is relatively robust with regards to hydrodynamic instabilities during the shell acceleration. Crucially, because the implosion velocity is less than that required for conventional compression ignition, considerably more fuel mass may be assembled for the same kinetic energy in the shell, offering significantly higher fusion yields for the same laser energy [4].

On the other hand, the laser spike intensity in the coronal plasma is above the threshold of parametric instabilities, thus the collisional absorption of laser light becomes inefficient and strong non-linear effects play an important role. These manifest themselves in enhanced scattering, accompanied by the generation of a population of hot electrons [15]. An understanding of the parametric instabilities and developing ways to control it are of great importance to the ultimate goal of achieving inertial confinement fusion in the laboratory.

Chapter 2

Laser-plasma interaction

When a high-power laser pulse is focused onto the surface of a solid target, a high density plasma layer is produced almost immediately. At the higher irradiances, the electric field of the laser light is sufficient to directly ionize the atoms. At the lower irradiances, the process is more complicated but nonetheless a plasma is produced rapidly. The whole region dominated by laser-plasma interactions, which is called corona, expands radially outwards at sonic velocities.

In the inertial fusion experiments, it is essential to deliver the laser energy into the capsule of fusion fuel as much as possible. However, the efficient transport of radiation within the target strongly depends on non-linear processes that take place during the propagation of the laser light in the coronal plasma. Therefore, laser-plasma interactions provide a key gateway to the study of inertial confinement fusion. A brief introduction to this exciting field, which is rich both in physics and in applications is provided in the following chapter.

2.1 Introduction to plasma physics

A plasma, one of the four fundamental states of matter, is a quasi-neutral gas of charged and neutral particles which exhibits collective behavior. It is necessary to explain some terms used in this definition.

By collective behavior one means motions that depend not only on local conditions but on the state of the plasma in remote regions as well. As charged particles move around, they can generate local concentrations of positive or negative charge, which give rise to electric fields. Motion of charges also generates currents, and hence magnetic fields. These fields affect the motion of other charged particles far away. Thus, the plasma gets a wide range of possible motions.

Quasi-neutrality describes the apparent charge neutrality of a plasma over large volumes, while at smaller scales, there can be charge imbalance, which may give rise to electric fields.

This fact can be expressed mathematically as

$$\sum_s q_s n_s \approx 0, \tag{2.1}$$

where q_s and n_s is, respectively, the charge and density of particles of species s. The index of summation is taken over all the particle species in plasma.

One of the most important parameters, which allows us to more accurately predict the behavior of plasmas, is the degree of its ionization. For a gas containing only single atomic species in thermodynamic equilibrium, the ionization can be clearly recognized from the Saha-Langmuir equation, which can be written in the following form,

$$\frac{n_{k+1}}{n_k} = \frac{2}{n_e h^3} (2\pi m_e k_B T)^{\frac{3}{2}} \frac{g_{k+1}}{g_k} \exp\left(-\frac{\varepsilon_{k+1} - \varepsilon_k}{k_B T}\right). \tag{2.2}$$

Here n_k is the density of atoms in the k-th state of ionization, n_e is the electron density, m_e stands for the mass of electron, k_B is Boltzmann's constant, T is the gas temperature, h is Planck's constant, g_k is the degeneracy of the energy level for ions in the k-th state, ε_k is the ionization energy of the k-th level. It can be clearly seen from equation (2.2) that the fully ionized plasmas exist only at high temperatures. That is the reason why plasmas do not occur naturally on Earth (with a few exceptions).

A fundamental characteristic of the behavior of a plasma is its ability to shield out electric potentials that are applied to it. Therefore, another important quantity λ_{Ds} which is called the Debye length of species s is established,

$$\lambda_{Ds} = \sqrt{\frac{\varepsilon_0 k_B T_s}{q_s^2 n_s}}. \tag{2.3}$$

The physical constant ε_0 is commonly called the permittivity of free space and T_s denotes the temperature of particles of species s. It often happens that the different species of particles in plasma have separate distributions with different temperatures, however each species can be in its own thermal equilibrium. The Debye length is a measure of the shielding distance or thickness of the sheath.

In plasma, each particle tries to gather its own shielding cloud. The previously mentioned concept of Debye shielding is valid only if there are enough particles in that cloud. Therefore, another important dimensionless number N_{Ds}, which is called plasma parameter of species s, is established. Definition of this parameter is given by the average number of particles of species s in a plasma contained within a sphere of radius of the Debye length, thus

$$N_{Ds} = \frac{4}{3}\pi n_s \lambda_{Ds}^3. \tag{2.4}$$

Consider an electrically neutral plasma in equilibrium. Suppose an amount of electrons

is displaced with respect to the ions, for example by intense laser pulse, and then allowed to move freely. An electric field will be set up, causing the electrons to be pulled back toward ions. Thus, the net result is a harmonic oscillation. The frequency of the oscillation is called the electron plasma frequency ω_{pe},

$$\omega_{pe} = \sqrt{\frac{e^2 n_e}{\varepsilon_0 m_e}}. \tag{2.5}$$

By analogy with the electron plasma frequency (2.5) one could define the ion plasma frequency ω_{pi} for a general ion species. However, the ions are much heavier than electrons, so they do not response to high frequency oscillation of electromagnetic field. It is often possible to treat the massive ions as an immobile, uniform, neutralizing background. However, if the frequency of external radiation source or the waves induced in plasmas is close to this frequency, the ion motion must also be included. An example may be stimulated Brillouin scattering, which derivation can be found at the end of this chapter.

A typical charged particle in a plasma simultaneously undergo Coulomb collisions with all of the other particles in the plasma. The importance of collisions is contained in an expression called the collision frequency ν_c, which is defined as the inverse of the mean time that it takes for a particle to suffer a collision. Relatively accurate calculation of electron-ion collision frequency ν_{ei} can be obtained from the following relation,

$$\nu_{ei} = \frac{Z e^4 n_e}{4\pi\varepsilon_0^2 m_e^2 v^3} \ln\Lambda, \qquad \Lambda = \frac{\lambda_D}{b_0}. \tag{2.6}$$

The coefficient Z denotes the charge number, v is relative velocity of colliding particles and $\ln\Lambda$ is the so-called Coulomb logarithm. It is ratio of the Debye to Landau length. Landau length b_0 is the impact parameter at which the scattering angle in the center of mass frame is 90°. For many plasmas of interest Coulomb logarithm takes on values between $5-15$. In a plasma a Coulomb collision rarely results in a large deflection. The cumulative effect of the many random small angle collisions that it suffers, however, is often larger than the effect of the few large angle collisions.

In a constant and uniform magnetic field one can find that a charged particle spirals in a helix about the line of force. This helix, however, defines a fundamental time unit and distance scale,

$$\omega_{cs} = \frac{|q_s| \|\mathbf{B}\|}{m_s}, \qquad r_{Ls} = \frac{v_\perp}{\omega_{cs}}. \tag{2.7}$$

These are called the cyclotron frequency ω_{cs} and the Larmor radius r_{Ls} of species s. Here $\mathbf{B}$ is a magnetic field and $v_\perp$ is a positive constant denoting the speed in the plane perpendicular to $\mathbf{B}$. Symbol $\|.\|$ stands for the Euclidean norm.

2.2 Description of plasma

There are basically three different approaches to plasma physics: the hydrodynamic theory, the kinetic theory and the particle theory. Each approach has some advantages and limitations which stems from simplified assumptions appropriate only for certain phenomena and time scales.

The plasma kinetic theory takes into account the motion of all of the particles. This can be done in an exact way, using Klimontovich equation. However, one is not usually interested in the exact motion of the particles, but rather in certain average characteristics. Thus, this equation can be good starting point for the derivation of approximate equations.

The kinetic theory is based on a set of equations for the distribution functions $f_s(\mathbf{x}, \mathbf{v}, t)$ of each plasma particle species s, together with Maxwell equations. Here $\mathbf{x}$ is the vector of coordinates for all the degrees of freedom, $\mathbf{v}$ is the corresponding vector of velocities and t is time. The distribution function is a statistical description of a very large number of interacting particles. If collisions can be neglected (for example in hot plasmas), the evolution of such a system can be described by the collisionless Vlasov equation,

$$\frac{\partial f_s}{\partial t} + \mathbf{v} \cdot \nabla f_s + \frac{q_s}{m_s} (\mathbf{E} + \mathbf{v} \times \mathbf{B}) \cdot \frac{\partial f_s}{\partial \mathbf{v}} = 0. \tag{2.8}$$

Here $\mathbf{E}$ and $\mathbf{B}$ are macroscopic electric and magnetic fields acting on the particles.

The equation (2.8) is obtained only by making the assumption that the particle density is conserved, such that the rate of change in a phase-space volume is equal to the flux of particles into that volume. Because of its comparative simplicity, this equation is most commonly used in kinetic theory. However, the assumption to neglect collisions in a plasma is not generally valid. If it is necessary to take them into account, the collision term can be approximated under certain conditions.

The second approach is hydrodynamic theory. In this model, the conservation laws of mass, momentum and energy are coupled to Maxwell equations. The fluid theory is the simplest description of a plasma, however this approximation is sufficiently accurate to describe the majority of observed phenomena. The velocity distribution of each species is assumed to be Maxwellian everywhere, so the dependent variables are functions of only space coordinates and time. The fluid equations are simply the first three moments of the Vlasov equation. These yield the following fluid equations for the density, the momentum and the energy,

$$\frac{\partial n_s}{\partial t} + \nabla \cdot (n_s \mathbf{u}_s) = 0, \tag{2.9}$$

$$m_s n_s \left[\frac{\partial \mathbf{u}_s}{\partial t} + (\mathbf{u}_s \cdot \nabla) \mathbf{u}_s \right] + \nabla \cdot \mathbb{P}_s = q_s n_s (\mathbf{E} + \mathbf{u}_s \times \mathbf{B}), \tag{2.10}$$

$$\frac{\partial}{\partial t} \left(\frac{1}{2} n_s m_s u_s^2 + e_s \right) + \nabla \cdot \left(\frac{1}{2} n_s m_s u_s^2 \mathbf{u}_s + e_s \mathbf{u}_s + \mathbb{P}_s \mathbf{u}_s + \mathbf{Q}_s \right) = q_s n_s \mathbf{u}_s \cdot \mathbf{E}. \tag{2.11}$$

The zeroth-order moment (2.9) gives the continuity equation, where $\mathbf{u}_s(\mathbf{x}, t)$ is the velocity of the fluid of species s. This equation essentially states that the total number of particles is conserved. The first-order moment (2.10) leads to a momentum equation. Here $\mathbb{P}_s(\mathbf{x}, t)$ is the pressure tensor. This comes about by separating the particle velocity into the fluid and a thermal component of velocity. The thermal velocity then leads to the pressure term. Finally, the second-order moment (2.11) corresponds to the energy equation, where e_s is the density of the internal energy and $\mathbf{Q}_s$ describes the heat flux density.

The moment equations are an infinite set of equations and a truncation is required in order to solve these equations. For this equation system to be complete it has to be supplemented by an equation of state, which describes the relation between pressure and density in the plasma. However, the equations of state are well defined only in local thermodynamic equilibrium. Otherwise, the system cannot be described by fluid equations.

The last possible description is the particle theory approach. The plasma is described by electrons and ions moving under the influence of the external (e.g. laser) fields and electromagnetic fields due to their own charge. The basic equation of motion for a charged particle in an electromagnetic field is given by the Newton equations of motion with the Lorentz force,

$$\frac{\mathrm{d}\mathbf{x}}{\mathrm{d}t} = \mathbf{v}, \qquad \frac{\mathrm{d}\mathbf{v}}{\mathrm{d}t} = \frac{q_s}{m_s} (\mathbf{E} + \mathbf{v} \times \mathbf{B}). \tag{2.12}$$

However, plasmas typically consist of an extremely large number of particles that interact in self-consistent fields, so the analysis can be applied only with the help of powerful computing infrastructure and particle simulation codes.

2.3 Electromagnetic waves in plasmas

In this section, some general properties of electromagnetic waves propagation in magnetized plasmas are described. Particularly, consider in some detail the waves traveling parallel to and perpendicular to magnetic field.

First, the dispersion relation is derived from the hydrodynamic plasma equations. Since we assume plasma response to a high frequency field, the ions are treated as stationary, neutralizing background. Thermal motion of particles is also ignored, thus the pressure term can be neglected. The following set of equations has to be solved,

$$\frac{\partial n_e}{\partial t} + \nabla \cdot (n_e \mathbf{u}_e) = 0, \tag{2.13}$$

$$m_e n_e \frac{\partial \mathbf{u}_e}{\partial t} + m_e n_e (\mathbf{u}_e \cdot \nabla) \mathbf{u}_e = -e n_e (\mathbf{E} + \mathbf{u}_e \times \mathbf{B}). \tag{2.14}$$

The symbol e denotes the elementary charge. To develop wave equations for the oscillating

electric and magnetic field, Faraday's law and Ampere's law are needed,

$$\frac{\partial \mathbf{B}}{\partial t} = -\nabla \times \mathbf{E}, \qquad \frac{\partial \mathbf{E}}{\partial t} = \frac{1}{\varepsilon_0 \mu_0} \nabla \times \mathbf{B} + \frac{e n_e \mathbf{u}_e}{\varepsilon_0}. \tag{2.15}$$

where μ_0 is permeability of free space.

Next, the system of equations will be linearized by using the methods of perturbation theory. Consider a small perturbations,

$$n_e = n_{e0} + \delta n_e, \quad \mathbf{u}_e = \delta \mathbf{u}_e, \quad \mathbf{B} = \mathbf{B}_0 + \delta \mathbf{B}, \quad \mathbf{E} = \delta \mathbf{E}. \tag{2.16}$$

After substituting perturbations into initial system of equations and performing Fourier transform one obtains

$$\delta n_e = \mathrm{i} \frac{n_{e0}}{\omega} \mathbf{k} \cdot \delta \mathbf{u}_e, \tag{2.17}$$

$$\delta \mathbf{u}_e = -\mathrm{i} \frac{e}{m_e \omega} \delta \mathbf{E} - \mathrm{i} \frac{e}{m_e \omega} \delta \mathbf{u}_e \times \mathbf{B}_0, \tag{2.18}$$

$$\delta \mathbf{B} = \frac{1}{\omega} \mathbf{k} \times \delta \mathbf{E}, \tag{2.19}$$

$$\delta \mathbf{E} = -\frac{1}{\varepsilon_0 \mu_0 \omega} \mathbf{k} \times \delta \mathbf{B} + \mathrm{i} \frac{e n_0}{\varepsilon_0 \omega} \delta \mathbf{u}_e, \tag{2.20}$$

where i denotes imaginary unit, $\mathbf{k}$ is wave vector and ω is angular frequency.

Equation for density perturbation can be ignored. Eliminating $\delta \mathbf{B}$ and $\delta \mathbf{u}_e$ from the equation (2.20) one gets the equation for perturbation of electric field,

$$\begin{aligned} \left(\omega^2 - \omega_{pe}^2 - c^2 k^2\right) \delta \mathbf{E} + \mathrm{i} \frac{\omega_{ce}}{\omega} \left(\omega^2 - c^2 k^2\right) \delta \mathbf{E} \times \mathbf{e}_B + \\ + c^2 \left(\mathbf{k} \cdot \delta \mathbf{E}\right) \mathbf{k} + \mathrm{i} \frac{\omega_{ce}}{\omega} c^2 \left(\mathbf{k} \cdot \delta \mathbf{E}\right) \mathbf{k} \times \mathbf{e}_B = 0. \end{aligned} \tag{2.21}$$

Here c is the speed of light in free space and $\mathbf{e}_B$ is a unit vector in the direction of the magnetic field,

$$c^2 = \frac{1}{\varepsilon_0 \mu_0}, \qquad \mathbf{e}_B = \frac{\mathbf{B}_0}{B_0}. \tag{2.22}$$

If one choose the coordinate system, where $\mathbf{B}_0 = (0, 0, B_0)$ and $\mathbf{k} = (k \sin\alpha, 0, k \cos\alpha)$, one obtain equation $\mathbb{M} \cdot \delta \mathbf{E} = 0$, where

$$\mathbb{M} = \begin{pmatrix} \omega^2 - \omega_{pe}^2 - c^2 k^2 \cos^2\alpha & \mathrm{i} \frac{\omega_{ce}}{\omega} \left(\omega^2 - c^2 k^2\right) & c^2 k^2 \cos\alpha \sin\alpha \\ -\mathrm{i} \frac{\omega_{ce}}{\omega} \left(\omega^2 - c^2 k^2 \cos^2\alpha\right) & \omega^2 - \omega_{pe}^2 - c^2 k^2 & -\mathrm{i} \frac{\omega_{ce}}{\omega} c^2 k^2 \cos\alpha \sin\alpha \\ c^2 k^2 \cos\alpha \sin\alpha & 0 & \omega^2 - \omega_{pe}^2 - c^2 k^2 \sin^2\alpha \end{pmatrix}. \tag{2.23}$$

The system of equations has non-trivial solution if and only if $\det \mathbb{M} = 0$. This condition leads to desired dispersion relation for an arbitrary angle α,

$$\begin{aligned} &\left[\left(\omega^2 - \omega_{pe}^2 - c^2 k^2 \cos^2\alpha\right)\left(\omega^2 - \omega_{pe}^2 - c^2 k^2 \alpha\right) - \left(\frac{\omega_{ce}}{\omega}\right)^2 \left(\omega^2 - c^2 k^2\right)\left(\omega^2 - c^2 k^2 \cos^2\alpha\right)\right] \\ &\left(\omega^2 - \omega_{pe}^2 - c^2 k^2 \sin^2\alpha\right) - c^4 k^4 \cos^2\alpha \sin^2\alpha \left[\left(\omega^2 - \omega_{pe}^2 - c^2 k^2\right) - \left(\frac{\omega_{ce}}{\omega}\right)^2 \left(\omega^2 - c^2 k^2\right)\right] = 0. \end{aligned} \tag{2.24}$$

Now, it is necessary to find a dispersion relations for the two simplest cases, propagation along and perpendicular to magnetic field. For the waves propagating along $\mathbf{B_0}$ is $\alpha = 0$ and dispersion relation (2.24) gets relatively simple form,

$$\left(\omega^2 - \omega_{pe}^2\right)\left[\left(\omega^2 - \omega_{pe}^2 - c^2 k^2\right)^2 - \left(\frac{\omega_{ce}}{\omega}\right)^2 \left(\omega^2 - c^2 k^2\right)^2\right] = 0. \tag{2.25}$$

The equation (2.25) has three solutions. The first describes plasma oscillations at frequency $\omega = \omega_{pe}$. The second and third solutions give right-handed (R) and left-handed (L) circularly polarized waves,

$$N_R^2 = 1 - \frac{\left(\omega_{pe}/\omega\right)^2}{1 - \omega_{ce}/\omega}, \qquad N_L^2 = 1 - \frac{\left(\omega_{pe}/\omega\right)^2}{1 + \omega_{ce}/\omega}. \tag{2.26}$$

The symbol N stands for the index of refraction, which is more useful for describing how waves propagate through medium.

In a similar manner, for the waves propagating perpendicular to $\mathbf{B_0}$ is $\alpha = \pi/2$ and the dispersion relation (2.24) has the following form,

$$\left(\omega^2 - \omega_{pe}^2 - c^2 k^2\right)\left[\left(\omega^2 - \omega_{pe}^2\right)\left(\omega^2 - \omega_{pe}^2 - c^2 k^2\right) - \omega_{ce}^2 \left(\omega^2 - c^2 k^2\right)\right] = 0. \tag{2.27}$$

The equation (2.27) has two solutions, which give ordinary (O) and extraordinary (X) waves,

$$N_O^2 = 1 - \left(\frac{\omega_{pe}}{\omega}\right)^2, \qquad N_X^2 = 1 - \left(\frac{\omega_{pe}}{\omega}\right)^2 \frac{1 - \left(\omega_{pe}/\omega\right)^2}{1 - \left(\omega_{pe}/\omega\right)^2 - \left(\omega_{ce}/\omega\right)^2} \tag{2.28}$$

The ordinary wave corresponds to a linearly polarized wave with electric field lying along the magnetic field direction, so that the motion remains unaffected. The extraordinary wave have electric fields that are perpendicular to magnetic field, but with components both perpendicular and parallel to the wave vector.

The important properties of these waves are distinguished by their cut-offs ($N \to 0$) and resonances ($N \to \infty$). In the vicinity of the resonance there is a total absorption, at a cut-off frequency there is a total reflection of incident waves. All of the cut-offs and resonances of waves are listed in table (1).

Wave	Cut-offs	Resonances
R	$\omega_R = \frac{1}{2}\omega_{ce} + \frac{1}{2}\sqrt{\omega_{ce}^2 + 4\omega_{pe}^2}$	$\omega_{ce} = \frac{eB_0}{m_e}$
L	$\omega_L = -\frac{1}{2}\omega_{ce} + \frac{1}{2}\sqrt{\omega_{ce}^2 + 4\omega_{pe}^2}$	$\omega_{ci} = \frac{ZeB_0}{m_i}$
O	$\omega = \sqrt{\omega_{pe}^2 + \omega_{pi}^2}$	$\omega_{uh} = \sqrt{\omega_{pe}^2 + \omega_{ce}^2}$
X	$\omega = \omega_R, \omega_L$	$\omega_{lh} = \sqrt{\omega_{ce}\,\omega_{ci}}$

Table 1: Summary of cut-offs and resonances for the principal waves

2.4 Laser absorption processes

Absorption of laser energy in laser-plasma interactions is an important issue, which has been closely related to the applications including the inertial fusion research ever since the invention of laser. Intense laser pulse can be absorbed in plasma by different non-linear mechanisms. In the following, the three main mechanisms of absorption of laser radiation are briefly described.

2.4.1 Collisional absorption

One of the most important mechanism of laser light absorption in plasma is collisional absorption, also called inverse bremsstrahlung. It is a process in which an electron absorbs a photon while colliding with an ion or with another electron, and it leads to the heating of all particles in the interaction region. This way electromagnetic energy of the laser wave is transferred into the kinetic energy of plasma.

The change in laser intensity I, passing through plasma in the direction of x-axis, is given by

$$\frac{\mathrm{d}I}{\mathrm{d}x} = -\kappa I, \tag{2.29}$$

where κ is the spatial damping rate of the laser energy caused by collisional absorption. For a slab of plasma of length L, the absorption coefficient α_{abs} is given by

$$\alpha_{\mathrm{abs}} = 1 - \frac{I_{\mathrm{out}}}{I_{\mathrm{in}}} = 1 - \exp\left(-\int_0^L \kappa\,\mathrm{d}x\right). \tag{2.30}$$

Here I_{out} and I_{in} are the outgoing and the incoming laser intensities, respectively. The absorption coefficient for a linear and exponential density profiles is given by solving the integral (2.30) [8],

$$\alpha_{\mathrm{abs}} = 1 - \exp\left(-\frac{32}{15}\frac{\nu_{ei}(n_c)L}{c}\right) \qquad \text{for} \qquad n_e = n_c\left(1 - \frac{x}{L}\right), \tag{2.31}$$

$$\alpha_{\mathrm{abs}} = 1 - \exp\left(-\frac{8}{3}\frac{\nu_{ei}(n_c)L}{c}\right) \qquad \text{for} \qquad n_e = n_c \exp\left(-\frac{x}{L}\right). \tag{2.32}$$

where $\nu_{ei}(n_c)$ is the collision frequency evaluated at the critical density n_c, which is given by formula

$$n_c = \frac{\varepsilon_0 m_e \omega}{e^2}. \tag{2.33}$$

Notice that a significant fraction of the collisional absorption is from the region near the critical density. Collisional absorption is the preferred absorption mechanism for driving matter ablatively with laser beams. In the case of long laser pulse duration with relatively low intensity, collisional absorption can be very efficient.

2.4.2 Resonance absorption

Laser light in the plasma can be also absorbed by resonance absorption. It is a linear process in which an incident laser wave is partially absorbed by conversion into an electron wave at the critical density of plasma.

Resonance absorption takes place when a p-polarized laser pulse is obliquely incident on a plasma with an inhomogeneous density profile. A component of the laser wave electric field perpendicular to the target surface then resonantly excites an electron plasma wave also along the plasma density gradient, thus a part of the laser wave energy is transferred into the electrostatic energy of the electron plasma wave. This wave propagates into the underdense plasma and it is damped either by collision or collisionless damping mechanisms. Consequently, energy is further converted into thermal energy which heats the plasma.

In contrast to collisional absorption, resonance absorption is the main absorption process for high laser intensities and long wavelengths. The efficiency of resonance absorption can also be higher for hot plasma, low critical density, or short plasma scale-length.

2.4.3 Landau damping

Landau damping is a very efficient damping mechanism of longitudinal plasma waves, which may occur even in the absence of collisions. Consider ions as a stationary neutralizing background. Using a linearized version of the Vlasov equation (2.8), one can find dispersion

relation for electron plasma waves,

$$\omega^2 \approx \omega_{pe}^2 + 3\frac{\omega_{pe}^2}{\omega^2} v_{th}^2 k^2 + \mathrm{i}\pi \frac{\omega_{pe}^2 \omega^2}{k^2} \frac{\mathrm{d}\hat{f}_0}{\mathrm{d}v_x}\bigg|_{v_x = v_{ph}}, \tag{2.34}$$

where v_{th} and v_{ph} are, respectively, electron thermal velocity and phase velocity of the wave, and $\hat{f}_0(v_x)$ is the one-dimensional normalized distribution function in the zeroth-order approximation. The imaginary part in (2.34) expresses Landau damping.

Only if the velocity distribution is not constant, the collisionless energy exchange between the wave and the particles occurs. The particles with a velocity almost equal to the phase velocity of the wave v_{ph} can become resonant with the field and therefore can be either slowed down or accelerated.

Let $\hat{f}_0(v_x)$ be Maxwellian, then one can calculate the Landau damping rate γ_L, which is given by

$$\gamma_\mathrm{L} \approx -\sqrt{\frac{\pi}{2}} \frac{\omega_{pe}}{(k\lambda_D)^3} \exp\left(-\frac{1}{2(k\lambda_D)^2}\right). \tag{2.35}$$

Since γ_L is negative, there is without doubt a collisionless damping of plasma waves. As is evident from (2.35) this damping becomes important when the wavelength is comparable to the Debye length.

However, the main feature of collisionless heating mechanisms is that only a minority fraction of the plasma electrons acquires most of the absorbed energy. This means that, as a side effect, a population of hot electrons is created, which significantly preheats the plasma.

2.5 Non-linear processes and instabilities

Plasma is strongly non-linear medium. This means that it may be accompanied by very strong electric fields and its non-linearities can be excited easily. When laser pulse with intensity above certain threshold irradiates the plasma, a number of collective non-linear processes may occur which can either enhance or reduce the energy absorption. As discussed before, the knowledge of the penetration depth and absorbed fraction of the incident energy is of vital importance for inertial confinement fusion research.

The non-linear interaction is conveniently described in terms of light pressure and the ponderomotive force, which is introduced first. In the next section, the parametric instabilities are discussed as a consequence of non-linear coupling of electromagnetic laser waves to the plasma. The last section describes the laser beam filamentation and self-focusing.

2.5.1 Ponderomotive force

The ponderomotive force is a most important quantity in the interaction of high intensity laser pulses with plasma. It leads to a wide range of non-linear phenomena. For normal laser

light incidence on plasma, the ponderomotive force $\mathbf{f}_p$ per unit volume is given by

$$\mathbf{f}_p = -\frac{\omega_{pe}^2}{\omega^2} \nabla \frac{\varepsilon_0 \langle E^2 \rangle}{2}, \tag{2.36}$$

where the $\langle\ \rangle$ symbol denotes the time average over one laser oscillating period. Notice that in a homogeneous field this time-averaged force vanishes.

The ponderomotive force represents the gradient of the laser electric field acting in a way to push charged particles into regions of lower field amplitude. It is the result of the Lorentz force that works on a charged particles in the electromagnetic wave.

Since the mass of the ions is much higher than electrons, the ponderomotive force acting on the ions is negligible. However, the ponderomotive force exerted on the electrons is transmitted to the ions by the electric field, which is created due to charge separation in the plasma.

2.5.2 Parametric instabilities

A parametric instability is defined in general by the non-linear phenomenon where a periodic variation in the medium supports the excitation of waves at a different frequency. In the following section we describe these wave excitation processes in more detail.

The resonance conditions in the three-wave interactions, under which parametric instabilities may grow, can be written in the form of the energy and momentum conservation laws,

$$\omega_0 = \omega_1 + \omega_2, \qquad \mathbf{k}_0 = \mathbf{k}_1 + \mathbf{k}_2, \tag{2.37}$$

where index 0 denotes parameters of the incident so-called pumping laser wave, which provides the driving force to excite other wave modes in the plasma. Indices $1, 2$ stand for the parameters of the two daughter waves.

These conditions imply that parametric instabilities take place only if a certain relations between the incident pump wave and the plasma frequency are fulfilled. A pumping laser wave can induce the following parametric instabilities that directly correspond to a plasma domain, because the plasma frequency is determined by the density of the plasma. Depending on which types of waves are excited, either the reflectivity or the absorption can be enhanced:

1. A laser pump with frequency $\omega_0 \approx \omega_{pe}$ may decay into an electron wave and an ion wave, leading to laser absorption. This phenomena occurs near the critical density n_c of plasma and is known as parametric decay instability.
2. A laser pump with frequency $\omega_0 > \omega_{pe}$ may decay into an ion wave and another electromagnetic wave, leading to laser scattering, including backscattering. This phenomena occurs in the whole domain of underdense plasma and is known as stimulated Brillouin scattering.
3. A laser pump with frequency $\omega_0 = 2\omega_{pe}$ may decay into two electron waves, leading to

laser absorption. This phenomena occurs at $n_c/4$ and is known as two-plasmon decay instability.

4. A laser pump with frequency $\omega_0 \geqslant 2\omega_{pe}$ may decay into an electron wave and another electromagnetic wave, leading to laser scattering, including backscattering. This phenomena occurs in a plasma with density lower than $n_c/4$ and is known as stimulated Raman scattering.

Even if these conditions are fulfilled, however, these instabilities do not need to be present in a plasma. The intensity of the incoming laser wave has to exceed a certain threshold in order for the parametric instability to occur, because all waves in plasma are damped either by collision and collisionless processes. If the laser intensity is higher than this limit, the amplitude of the parametric decay mode increases.

2.5.3 Filamentation and self-focusing

The laser beam filamentation and self-focusing result from the same physical processes. These instabilities occur for densities less than the critical density where the laser beam couples to an ion acoustic perturbation. The filamentation and self-focusing correspond to the growth of zero-frequency density perturbations and are caused by variations in either the laser intensity across the beam regions or plasma density.

In the higher laser intensity region, plasma is pushed aside in the radial direction of the beam due to the ponderomotive force. This reduces the density locally and increases the index of refraction of the plasma. The resulting index of refraction is seen by the laser pulse as a focusing lens, thus prevents it from spreading. Consequently, the laser intensity increases there still further, which completes the unstable feedback loop.

Notice that in addition to ponderomotive driven filamentation and self-focusing, there is a variety of mechanism that leads to a change of the refractive index in laser-plasma interactions. These include the collisions, a thermal, or relativistic effects.

The undesirable effects of filamentation and self-focusing are induced instabilities which can produce hot electrons that preheat the fuel target core or reduce laser energy absorption. It is, of course, a serious problem in laser fusion research.

Chapter 3

Numerical simulations

The collective behavior of particles and fields in laser-plasma interactions represent a complex and strongly non-linear problem. The investigation of such systems cannot be carried out only through the application of two traditional techniques, namely, theoretical and experimental work. Since there is a large number of a very complex simultaneous interactions of a many degrees of freedom in plasma, analytical modeling seems to be impractical. On the other hand, many of the significant details of laser-plasma interaction are extremely difficult or even impossible to obtain experimentally. Therefore, for the further understanding in this field of research other tools and techniques are required [14].

Numerical simulation is now an integrated part of science and technology. With the advent of powerful computational systems, numerical simulations now play an important role in physics as an essential tool in developing theoretical models and understanding experimental results. Numerical simulation is now rightfully considered as a separate discipline from theory and experiment [23].

Numerical simulations help researchers to develop models covering a wide range of physical scenarios and to investigate their properties. For example, numerical schemes for Newton's equation can be implemented in the study of the molecular dynamic, the techniques used to solve hydrodynamic equations are needed in weather prediction and algorithms for solving the diffusion equation can be applied to air pollution control problems. Only one numerical code can solve a variety of physical problems by modification of the initial and boundary conditions. These so-called computer experiments are often faster and much cheaper than a single real experiment in laboratory [12].

Nowadays, it is clear that a detailed understanding of the physical mechanisms in laser-plasma interaction can only be achieved through the combination of theory, experiment and simulation. Development of parallel algorithms that lead to a stable and sufficiently exact solution, however, belong to the most challenging fields of modern science.

The most part of this chapter is focused on the description of the particle-in-cell method, which is the very popular numerical algorithm used for plasma simulations. There can be found the mathematical background of this method, description of the steps of the simulation

loop and stability conditions. The last section provides a brief overview of the particle-in-cell code EPOCH, which has been used for simulations within this work.

3.1 Particle-in-cell method

The particle-in-cell (PIC) method refers to a technique used to solve a certain class of partial differential equations. The method was proposed in the mid-fifties and it gained a great popularity in plasma physics applications early. It is based on the particle description approach, thus the evolution of the system is conducted in principle by following the trajectory of each particle.

However, the real systems are often extremely large in terms of the number of particles they contain. In order to make simulations efficient or at all possible, so-called macro-particles are used. A macro-particle is a finite-sized computational particle that represents a group of physical particles that are near each other in the phase space. It is allowed to rescale the number of particles, because the Lorentz force depends only on the charge to mass ratio, which is invariant to this transformation. Thus, a macro-particle will follow the same trajectory as the corresponding real particles would [13].

Although this approach significantly reduces the number of computational particles, the binary interactions for every pair of a system cannot be taken into account. The cost would scales quadratically, as the number of particles increases, which makes the computational effort unmanageable in the case of larger systems. Many of the phenomena occur in high-temperature plasmas where collisional effects are very weak, thus one can neglect them. Otherwise, one may use other techniques to include collisional effects [18].

Here, the procedure for deriving the PIC method is considered. The phase space distribution function $f_s(\mathbf{x}, \mathbf{v}, t)$ for a given species s is governed by the Vlasov equation (2.8) in the collisionless plasma. The PIC method can be regarded as a finite element approach but with finite elements that are themselves moving and overlapping. The mathematical formulation of the PIC method is obtained by assuming that the distribution function of each species is given by the sum of distribution functions for macro-particles,

$$f_s(\mathbf{x}, \mathbf{v}, t) = \sum_p f_p(\mathbf{x}, \mathbf{v}, t). \tag{3.1}$$

Index p denotes hereafter the quantities attributable to macro-particles. The distribution function for each macro-particle is further assumed to be

$$f_p(\mathbf{x}, \mathbf{v}, t) = N_p S_x(\mathbf{x} - \mathbf{x}_p(t)) S_v(\mathbf{v} - \mathbf{v}_p(t)), \tag{3.2}$$

where N_p is the number of physical particles that are represented by each macro-particle, and S_x, S_v are the so-called shape functions.

The shape functions cannot be chosen arbitrarily. They have to fulfill a several special

properties. Let S_ξ be the shape function of the phase space coordinate ξ. Then:

1. The support of the shape function is compact, $\exists R > 0$, supp $S_\xi \subset (-R, R)$.
2. Integral of the shape function is unitary, $\int_{-\infty}^{+\infty} S_\xi(\xi)\,\mathrm{d}\xi = 1$.
3. The shape function is symmetrical, $S_\xi(\xi) = S_\xi(-\xi)$.

While these restrictive conditions still offer a wide range of possibilities, the standard PIC method is essentially determined by the choice of the shape function in the velocity direction as a Dirac δ-function and in the spatial direction as a m-th order b-spline basis function b_m,

$$S_v(\mathbf{v} - \mathbf{v}_p(t)) = \delta(\mathbf{v} - \mathbf{v}_p(t)), \qquad S_x(\mathbf{x} - \mathbf{x}_p(t)) = b_m\left(\frac{\mathbf{x} - \mathbf{x}_p(t)}{\Delta p}\right), \tag{3.3}$$

where Δp is the size of the support of the computational particles, typically the same as simulation grid cell. Stability and accuracy of the simulation strongly depend on the choice of the shape functions. The choice of higher-order basis functions results in less numerical noise interpolation of density and field quantities and reduces non-physical phenomena in simulations, obviously at the cost of increased computational time.

The computational cycle of the PIC method is shown in Figure 1. Individual steps are closer described in several following sections. The influence of the choice of the time and spatial step on the stability and accuracy of the PIC method is demonstrated in the last section.

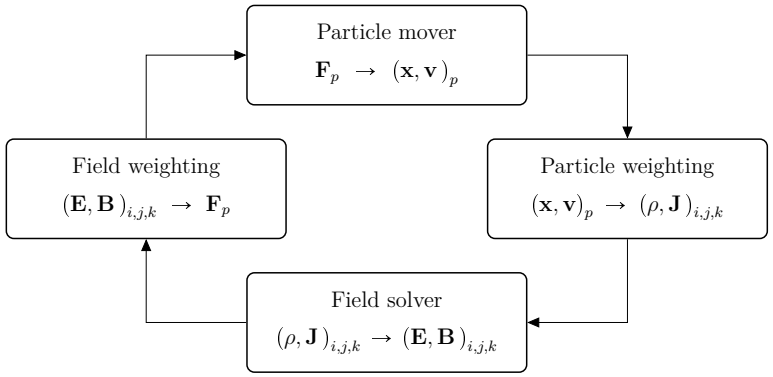

Figure 1: Computational cycle of the particle-in-cell method

3.1.1 Field solver

The behavior of the time varying electromagnetic field in the free space is governed by the microscopic variant of Maxwell equations,

$$\nabla \cdot \mathbf{E} = \frac{\rho}{\varepsilon_0}, \qquad \nabla \cdot \mathbf{B} = 0 \tag{3.4}$$

$$\nabla \times \mathbf{E} = -\frac{\partial \mathbf{B}}{\partial t}, \qquad \nabla \times \mathbf{B} = \mu_0 \mathbf{J} + \frac{1}{c^2}\frac{\partial \mathbf{E}}{\partial t}, \tag{3.5}$$

where $\rho(\mathbf{x}, t)$ is charge density and $\mathbf{J}(\mathbf{x}, t)$ current density.

To make the simulation possible, PIC method solves field equations only at certain points of the computational domain and time levels. Therefore, it is necessary to perform the discretization of the spatial coordinates $\mathbf{x} \to x_{i,j,k}$ where $(i, j, k) \in \mathbb{N}^3$ are grid indices and the time coordinate $t \to t^n$, where $n \in \mathbb{N}$ is the time level index. Solution is outlined here for a three-dimensional equidistant rectangular grid, thus $x_{i,j,k} = (i\Delta x, j\Delta y, k\Delta z)$ where $\Delta x, \Delta y, \Delta z$ are the spatial steps in each direction and $t^n = n\Delta t$ where Δt is the time step.

Typical method to solve Maxwell equations in PIC codes is finite-difference time-domain (FDTD), because it is arguably the simplest technique in terms of the implementation. The vector components of the fields $\mathbf{E}$ and $\mathbf{B}$ are spatially staggered about rectangular unit cells of a Cartesian computational grid,

$$\mathbf{E}(\mathbf{x}, t) \to \left[(E_x)^n_{i,\, j+1/2,\, k+1/2}, (E_y)^n_{i+1/2,\, j,\, k+1/2}, (E_z)^n_{i+1/2,\, j+1/2,\, k} \right], \tag{3.6}$$

$$\mathbf{B}(\mathbf{x}, t) \to \left[(B_x)^n_{i+1/2,\, j,\, k}, (B_y)^n_{i,\, j+1/2,\, k}, (B_z)^n_{i,\, j,\, k+1/2} \right]. \tag{3.7}$$

This scheme, which has proven to be very robust, is now known as a Yee lattice [29]. The illustration of a standard Cartesian Yee cell used for FDTD is shown in Figure 2. Components of the current density $\mathbf{J}$ are defined in the same way as the components of $\mathbf{E}$, charge density is defined in the middle of the cell. For marching in time a leap-frog scheme is used, thus discretized Maxwell equations (3.4), (3.5) have the following form,

$$\nabla^+ \cdot \mathbf{E}^n = \frac{\rho^n}{\varepsilon_0}, \quad \nabla^- \cdot \mathbf{B}^{n+1/2} = 0. \tag{3.8}$$

$$\frac{\mathbf{B}^{n+1/2} - \mathbf{B}^{n-1/2}}{\Delta t} = -\nabla^- \times \mathbf{E}^n, \quad \frac{1}{c^2}\frac{\mathbf{E}^{n+1} - \mathbf{E}^n}{\Delta t} = \nabla^+ \times \mathbf{B}^{n+1/2} - \mu_0 \mathbf{J}^{n+1/2}, \tag{3.9}$$

Notice that FDTD method achieve second-order accuracy in both, space and time. Discrete operators (∇^+) and (∇^-) act on a scalar field $f_{i,j,k}$,

$$\nabla^+ f_{i,\,j,\,k} = \left(\frac{f_{i+1,\,j,\,k} - f_{i,\,j,\,k}}{\Delta x}, \frac{f_{i,\,j+1,\,k} - f_{i,\,j,\,k}}{\Delta y}, \frac{f_{i,\,j,\,k+1} - f_{i,\,j,\,k}}{\Delta z} \right), \tag{3.10}$$

$$\nabla^- f_{i,\,j,\,k} = \left(\frac{f_{i,\,j,\,k} - f_{i-1,\,j,\,k}}{\Delta x}, \frac{f_{i,\,j,\,k} - f_{i,\,j-1,\,k}}{\Delta y}, \frac{f_{i,\,j,\,k} - f_{i,\,j,\,k-1}}{\Delta z} \right). \tag{3.11}$$

These operators have the following properties,

$$\nabla^- \cdot \nabla^- \times = \nabla^+ \cdot \nabla^+ \times = 0, \qquad \nabla^- \cdot \nabla^+ = \nabla^+ \cdot \nabla^- = \Delta. \tag{3.12}$$

Symbol Δ stands for the discrete Laplace operator in central differences,

$$\Delta f_{i,j,k} = \frac{f_{i-1,j,k} + 2f_{i,j,k} + f_{i+1,j,k}}{\Delta x^2} + \frac{f_{i,j-1,k} + 2f_{i,j,k} + f_{i,j+1,k}}{\Delta y^2} + \frac{f_{i,j,k-1} + 2f_{i,j,k} + f_{i,j,k+1}}{\Delta z^2}. \tag{3.13}$$

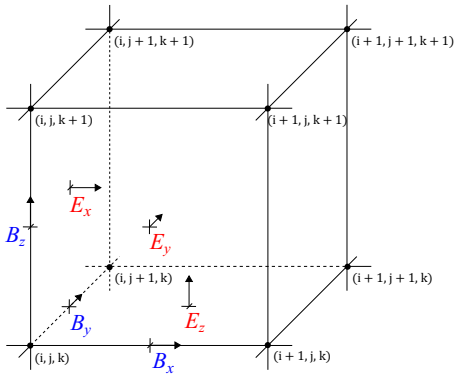

Figure 2: Standard Cartesian Yee cell used for FDTD method

Before trying to find the solution of Maxwell equations, one have to realize that this system of equations is not independent. In the three-dimensional case, there are eight first-order differential equations, but only six unknown vector components. Acting on the first and second of the equations (3.9) by operators $(\nabla^- \cdot)$ and $(\nabla^+ \cdot)$, respectively, one obtains

$$\frac{\nabla^- \cdot \mathbf{B}^{n+1/2} - \nabla^- \cdot \mathbf{B}^{n-1/2}}{\Delta t} = 0, \tag{3.14}$$

$$\frac{\rho^{n+1} - \rho^n}{\Delta t} + \nabla^+ \cdot \mathbf{J}^{n+1/2} = 0. \tag{3.15}$$

It means that it is possible to solve only equations (3.9), while the divergence equations (3.8) can be considered as initial conditions. In this case, the continuity equation in finite differences (3.15) have to be fulfilled.

3.1.2 Particle and field weighting

The particle weighting refers to the part of the code in which the charge and current densities are assigned to the discrete grid points from the continuous particle positions. After the fields are obtained, they are assigned back at the particles to calculate the Lorentz force. This step is called field weighting. It implies some form of interpolation.

First, have a look at the particle weighting. Charge density $\rho(\mathbf{x},t)$ and current density $\mathbf{J}(\mathbf{x},t)$ are given by the following integrals over the velocity space,

$$\rho(\mathbf{x},t)=\sum_s q_s\int f_s(\mathbf{x},\mathbf{v},t)\,\mathrm{d}\mathbf{v},\qquad \mathbf{J}(\mathbf{x},t)=\sum_s q_s\int f_s(\mathbf{x},\mathbf{v},t)\,\mathbf{v}\,\mathrm{d}\mathbf{v}. \tag{3.16}$$

The interpolation function is defined as

$$W_{i,j,k}\left(\mathbf{x}_p^n\right)=\frac{1}{\Delta V}\int_\Omega S_x\left(\mathbf{x}-\mathbf{x}_p^n\right)\mathrm{d}\mathbf{x},\qquad \Delta V=\Delta x\Delta y\Delta z, \tag{3.17}$$

where $\Omega=\{\mathbf{x}\in\mathbb{R}^3:|x_1-x_{i,j,k}|\leqslant\Delta x/2\wedge|x_2-x_{i,j,k}|\leqslant\Delta y/2\wedge|x_3-x_{i,j,k}|\leqslant\Delta z/2\}$. Then the charge density $\rho_{i,j,k}^n$ in the arbitrary grid point $x_{i,j,k}$ and time level t^n is constructed as

$$\rho_{i,j,k}^n=\sum_p q_p W_{i,j,k}\left(\mathbf{x}_p^n\right),\qquad q_p=q_s N_p, \tag{3.18}$$

where the sum is taken over all computational particles.

By analogy, one could assign the current densities to the grid points using this interpolation function, but the discrete continuity equation for charge (3.15) would not be satisfied exactly. In this case one have to solve Poisson's equation for correction of electric field or use one of the several numerical schemes for computing the current density satisfying the continuity equation, which are called charge conservation methods. In the next paragraph, the charge density decomposition method proposed by Esirkepov [9] is described.

Due to linearity of the continuity equation (3.15), it is sufficient to define the current density associated with the motion of a single computational particle,

$$\begin{aligned}(J_x)_{i+1,\,j,\,k}^n&=(J_x)_{i,\,j,\,k}^n-q_p\,(v_x)_p^n\,(\Pi_x)_{i,\,j,\,k}^n,\\ (J_y)_{i,\,j+1,\,k}^n&=(J_y)_{i,\,j,\,k}^n-q_p\,(v_y)_p^n\,(\Pi_y)_{i,\,j,\,k}^n,\\ (J_z)_{i,\,j,\,k+1}^n&=(J_z)_{i,\,j,\,k}^n-q_p\,(v_z)_p^n\,(\Pi_z)_{i,\,j,\,k}^n.\end{aligned} \tag{3.19}$$

In accordance with continuity equation one can write

$$(\Pi_x)_{i,\,j,\,k}^n+(\Pi_y)_{i,\,j,\,k}^n+(\Pi_z)_{i,\,j,\,k}^n=W_{i,j,k}\left(\mathbf{x}_p^n+\tilde{\mathbf{x}}\right)-W_{i,j,k}\left(\mathbf{x}_p^n\right), \tag{3.20}$$

where $\tilde{\mathbf{x}}\in\mathbb{R}^3$ is the motion induced position shift of the computational particle in one simulation time step. Shift of the computational particle generates eight variants of interpolation functions,

$$\begin{aligned}&W_{i,j,k}\left(\mathbf{x}_p^n\right),\quad W_{i,j,k}\left(\mathbf{x}_p^n+\tilde{x}_1\right),\quad W_{i,j,k}\left(\mathbf{x}_p^n+\tilde{x}_2\right),\quad W_{i,j,k}\left(\mathbf{x}_p^n+\tilde{x}_3\right),\\ &W_{i,j,k}\left(\mathbf{x}_p^n+\tilde{x}_1+\tilde{x}_2\right),\quad W_{i,j,k}\left(\mathbf{x}_p^n+\tilde{x}_1+\tilde{x}_3\right),\quad W_{i,j,k}\left(\mathbf{x}_p^n+\tilde{x}_2+\tilde{x}_3\right),\\ &W_{i,j,k}\left(\mathbf{x}_p^n+\tilde{x}_1+\tilde{x}_2+\tilde{x}_3\right).\end{aligned} \tag{3.21}$$

We assume that the vector $\Pi_{i,\,j,\,k}^n$ is linearly dependent on the functions (3.21). It turned out that only one linear combination exists.

Now, have a look at the field weighting. After calculating Maxwell equations at the grid points, it is necessary to assign electric and magnetic fields back at the particle positions. Recall the definition of interpolation function (3.17). By analogy to the particle weighting, one can assign the components of electric field,

$$\begin{aligned}(E_x)_p^n&=\sum_{i,j,k}(E_x)_{i,\,j+1/2,\,k+1/2}^n\,W_{i,\,j+1/2,\,k+1/2}\left(\mathbf{x}_p^n\right),\\ (E_y)_p^n&=\sum_{i,j,k}(E_y)_{i+1/2,\,j,\,k+1/2}^n\,W_{i+1/2,\,j,\,k+1/2}\left(\mathbf{x}_p^n\right),\\ (E_z)_p^n&=\sum_{i,j,k}(E_z)_{i+1/2,\,j+1/2,\,k}^n\,W_{i+1/2,\,j+1/2,\,k}\left(\mathbf{x}_p^n\right),\end{aligned} \tag{3.22}$$

and the components of magnetic field,

$$\begin{aligned}(B_x)_p^n&=\sum_{i,j,k}(B_x)_{i+1/2,\,j,\,k}^n\,W_{i+1/2,\,j,\,k}\left(\mathbf{x}_p^n\right),\\ (B_y)_p^n&=\sum_{i,j,k}(B_y)_{i,\,j+1/2,\,k}^n\,W_{i,\,j+1/2,\,k}\left(\mathbf{x}_p^n\right),\\ (B_z)_p^n&=\sum_{i,j,k}(B_z)_{i,\,j,\,k+1/2}^n\,W_{i,\,j,\,k+1/2}\left(\mathbf{x}_p^n\right).\end{aligned} \tag{3.23}$$

It is desirable to use the same interpolation function for both, density and force calculations, in order to eliminate a self-force and ensure conservation of momentum [10].

3.1.3 Particle mover

The behavior of computational particles is controlled by the Newton-Lorentz equations. Since the particles can reach velocities near the velocity of light, it is necessary to perform relativistic generalization,

$$\mathbf{u}_p=\gamma\,\mathbf{v}_p,\qquad \gamma=\sqrt{1+\left(\frac{\mathbf{u}_p}{c}\right)^2}. \tag{3.24}$$

Assume that the electric and magnetic fields are interpolated from the grid points to the particles at the time level t^n. Then the computational particle equations of motion to be integrated are

$$\frac{\mathrm{d}\mathbf{x}_p}{\mathrm{d}t} = \frac{\mathbf{u}_p}{\gamma}, \qquad \frac{\mathrm{d}\mathbf{u}_p}{\mathrm{d}t} = \frac{q_s}{m_s}\left(\mathbf{E}_p + \frac{\mathbf{u}_p}{\gamma} \times \mathbf{B}_p\right). \tag{3.25}$$

To discretize equations of motion (3.25) a time-centered leap-frog scheme is used. One obtains

$$\frac{\mathbf{x}_p^{n+1} - \mathbf{x}_p^{n}}{\Delta t} = \frac{\mathbf{u}_p^{n+1/2}}{\gamma^{\,n+1/2}}, \tag{3.26}$$

$$\frac{\mathbf{u}_p^{n+1/2} - \mathbf{u}_p^{n-1/2}}{\Delta t} = \frac{q_s}{m_s}\left(\mathbf{E}_p^{\,n} + \frac{\mathbf{u}_p^{n+1/2} + \mathbf{u}_p^{n-1/2}}{2\gamma^{\,n}} \times \mathbf{B}_p^{\,n}\right). \tag{3.27}$$

Although these equations appear to be very simple, the solution is the most time-consuming part of the simulation, because they have to be solved for every single computational particle. Standard for particle pushing in plasma simulation PIC codes is elegant Boris method, which completely separates the effect of electric and magnetic fields [6]. Substitute

$$\mathbf{u}_p^{n-1/2} = \mathbf{u}_p^{-} - \frac{q_s\mathbf{E}_p^{\,n}}{m_s}\frac{\Delta t}{2}, \qquad \mathbf{u}_p^{n+1/2} = \mathbf{u}_p^{+} + \frac{q_s\mathbf{E}_p^{\,n}}{m_s}\frac{\Delta t}{2} \tag{3.28}$$

into equation (3.27), then the electric field cancels entirely,

$$\frac{\mathbf{u}_p^{+} - \mathbf{u}_p^{-}}{\Delta t} = \frac{q_s}{2\gamma^{\,n} m_s}\left(\mathbf{u}_p^{+} + \mathbf{u}_p^{-}\right) \times \mathbf{B}_p^{\,n}. \tag{3.29}$$

Equation (3.29) describes a rotation of vector $\mathbf{u}_p^{-}$ to $\mathbf{u}_p^{+}$ in one simulation time step Δt. The angle θ between vector $\mathbf{u}_p^{-}$ and $\mathbf{u}_p^{+}$ we expect to be $\theta = \omega_c \Delta t$.

To implement the Boris method, first add half the electric impulse $\mathbf{E}_p^{\,n}$ to $\mathbf{u}_p^{n-1/2}$, then perform the full rotation by the angle θ, and finally, add another half the electric impulse $\mathbf{E}_p^{n}$. From the basic geometry Boris derived following steps to obtain $\mathbf{u}_p^{n+1/2}$. From the first of equations (3.28) express vector $\mathbf{u}_p^{-}$,

$$\mathbf{u}_p^{-} = \mathbf{u}_p^{n-1/2} + \frac{q_s\mathbf{E}_p^{\,n}}{m_s}\frac{\Delta t}{2} \tag{3.30}$$

and construct an auxiliary vector $\mathbf{u}_p'$, which is simultaneously perpendicular to $\left(\mathbf{u}_p^{+} - \mathbf{u}_p^{-}\right)$ and to $\mathbf{B}_p^{\,n}$,

$$\mathbf{u}_p' = \mathbf{u}_p^{-} + \mathbf{u}_p^{-} \times \mathbf{t}, \qquad \mathbf{t} = \frac{q_s\mathbf{B}_p^{\,n}\Delta t}{2\gamma^{\,n} m_s}. \tag{3.31}$$

Vector $\mathbf{t}$ has to be logically parallel to $\mathbf{B}_p^{\,n}$ with the length of $\tan(\theta/2) \approx \theta/2$ for small angles.

Next, utilize the fact that the vector $(\mathbf{u}_p' \times \mathbf{B}_p^{\,n})$ is parallel to $\left(\mathbf{u}_p^{+} - \mathbf{u}_p^{-}\right)$ and express $\mathbf{u}_p^{+}$,

$$\mathbf{u}_p^{+} = \mathbf{u}_p^{-} + \mathbf{u}_p' \times \mathbf{s}, \qquad \mathbf{s} = \frac{2\mathbf{t}}{1+t^2}. \tag{3.32}$$

Here vector $\mathbf{s}$ is parallel to $\mathbf{B}_p^{\,n}$ and its length has to fulfill the condition $\|\mathbf{u}_p^{+}\| = \|\mathbf{u}_p^{-}\|$. The transition from $\mathbf{u}_p^{-}$ to $\mathbf{u}_p^{+}$ can be written more clearly using the matrix,

$$\mathbf{u}_p^{+} = \begin{pmatrix} 1 - s_2t_2 - s_3t_3 & s_2t_1 + s_3 & s_3t_1 - s_2 \\ s_1t_2 - s_3 & 1 - s_1t_1 - s_3t_3 & s_3t_2 + s_1 \\ s_1t_3 + s_2 & s_2t_3 - s_1 & 1 - s_1t_1 - s_2t_2 \end{pmatrix} \mathbf{u}_p^{-}. \tag{3.33}$$

Finally, substitute vector $\mathbf{u}_p^{+}$ into the second from the equations (3.28),

$$\mathbf{u}_p^{n+1/2} = \mathbf{u}_p^{+} + \frac{q_s\mathbf{E}_p^{\,n}}{m_s}\frac{\Delta t}{2}. \tag{3.34}$$

The position of computational particle is advanced according to

$$\mathbf{x}_p^{n+1} = \mathbf{x}_p^{n} + \frac{\mathbf{u}_p^{n+1/2}}{\gamma^{\,n+1/2}}\Delta t, \qquad \gamma^{\,n+1/2} = \sqrt{1 + \left(\frac{\mathbf{u}_p^{n+1/2}}{c}\right)^2}. \tag{3.35}$$

3.1.4 Stability and accuracy

The stability and accuracy of the standard PIC method is directly dependent on the size of the spatial and temporal simulation steps. In order to find correct parameters one has to know the absolute accuracy and corresponding stability conditions.

The effect of the spatial grid is to smooth the interaction forces and to couple plasma perturbations to perturbations at other wavelengths, called aliases. It can lead to non-physical instabilities and numerical heating. To avoid these effect, the spatial step needs to resolve the Debye length. Thus, it is desirable to fulfill the following condition,

$$\Delta x \leqslant \lambda_D. \tag{3.36}$$

In general electromagnetic case, the time step has to satisfy the Courant–Fridrichs–Levy (CFL) condition [14],

$$C = c^2\Delta t^2\left(\frac{1}{\Delta x^2} + \frac{1}{\Delta y^2} + \frac{1}{\Delta z^2}\right). \tag{3.37}$$

where the dimensionless number $C \leqslant 1$ is called the CFL number. This condition limits

the range of motion of all objects in simulation during one time step. It ensures, that these particles will not cross more than one cell in one time step. When this condition is violated, the growth of non-physical effects can be very rapid.

The leap-frog scheme, used to solve the field equations and equations of motion, is second-order accurate in both, time and space. In addition, this scheme is explicit and time-reversible.

3.2 Code EPOCH

The abbreviation EPOCH refers to an Extendable PIC Open Collaboration project [1]. EPOCH is a multi-dimensional, relativistic, electromagnetic code for plasma physics simulations based on the PIC method. The code, which is developed in University of Warwick, is written in FORTRAN and parallelized using MPI library. EPOCH is explicit and is able to achieve second-order accuracy. The entire core of the code uses SI units.

The main features include dynamic load balancing option for making optimal use of all processors when run in parallel, allowing restart on an arbitrary number of processors. The setup of EPOCH is controlled through a customizable input deck. An input deck is text file which can be used to set simulation parameters for EPOCH without needing to edit or recompile the source code. Most aspects of a simulation can be controlled, such as the number of grid points in the simulation domain, the initial distribution of particles and the initial electromagnetic field configuration. In addition, EPOCH was written to add more modern features and to structure the code in such a way that the future expansion of the code may be made as easily as possible.

By default, EPOCH uses triangular particle shape functions with the peak located at the position of computational particle and a width of two cells, which provides relatively clean and fast solution. However, user can select higher order particle shape functions based on spline interpolation by enabling compile time option in the makefile.

The electromagnetic field solver uses a FDTD scheme with second order of accuracy. The field components are spatially staggered on a standard Cartesian Yee cell. The solver is directly based on the scheme derived by Hartmut Ruhl [11]. The particle pusher is relativistic, Birdsall and Landon type [6] and uses Villasenor and Buneman current weighting [28].

Chapter 4

Results

In this chapter, the achieved results of this work are presented and discussed. The code EPOCH, mentioned before, has been used for all simulations within this work. First, the boundary conditions for efficient absorption of hot electrons have been implemented and thoroughly tested in several test simulations. Second, two large-scale 2D simulations of laser-plasma interaction have been performed. The results have been post-processed and analyzed in terms of energy absorption efficiency, scattered radiation and production of hot electrons in the context of contemporary inertial fusion research.

4.1 Boundary conditions

The purpose of adding new boundary conditions to the code was to eliminate accumulation of the electromagnetic field at the boundary of the simulation domain (Figure 3-a), which was pushing the electrons back and caused non-physical phenomena, especially in longer simulations with higher intensities. To mitigate this non-physical effect, a new boundary condition has been implemented using the Monte Carlo method. Thus as electron moves towards the target core, there is an increasing probability that its energy will be decreased to the value corresponding to the initial temperature. This approach has an analogy in the thermalization process in dense plasmas. Many types of probability density functions have been tested. It turned out, that the best properties has a modified trigonometric function (Figure 3-b).

Boundary conditions have been tested recently using one-dimensional simulation code [20]. The laser pulse with $I\lambda^2 = 4,95 \cdot 10^{16}$ Wμm^2/cm^2 has been normally incident and p-polarized. The initial temperature has been chosen to 530 eV for electrons, 60 eV for ions. Coulomb collisions were neglected in these simulations. The behavior and effect of the implemented boundary condition can be observed in Figure 4. In ideal case, the distribution of particles forming the return current should be approximately Maxwellian with the initial temperature (Figure 4-b). Without this boundary condition, the energy spectrum of electrons

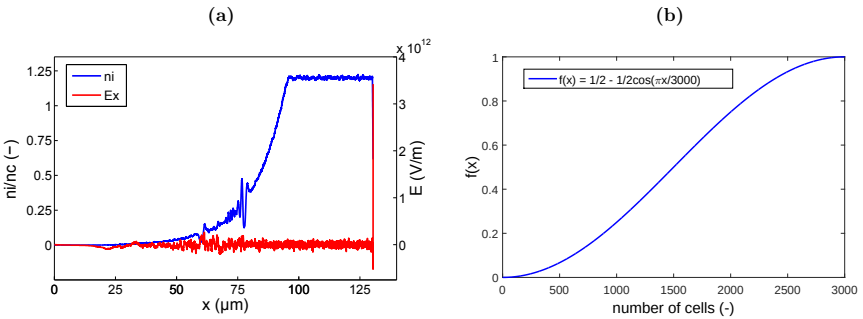

Figure 3: (a) Ion density profile (blue) and longitudinal electric field (red) at the time of 2500 laser periods in a test simulation of intense laser pulse interaction with plasma with the former absorbing boundary conditions. The plasma profile is exponential with the scale length of 10 laser wavelengths. The laser beam enters simulation domain on the left side, n_c stands for the critical density. **(b)** The function used for boundary condition. The condition is set on the last 3000 computational cells (laser wavelength corresponds to 120 cells).

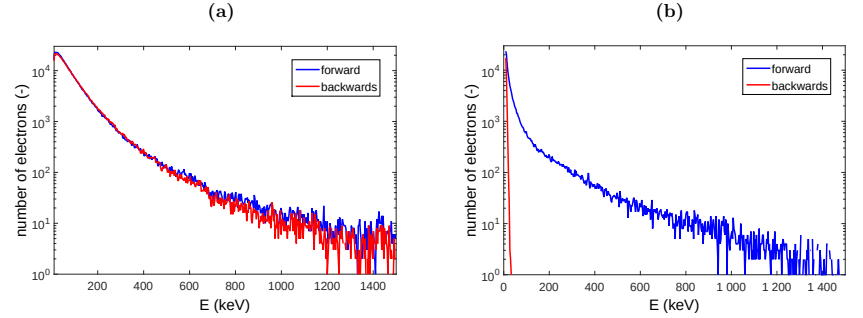

Figure 4: Energy distribution function of electrons recorded at the location of the boundary condition going into the target core (blue) and backwards (red). The former absorbing boundary condition is used in **(a)** while the newly implemented boundary condition is used in **(b)**. Other simulation parameters are the same as in Fig. 3.

propagating backwards is almost equal with spectrum of electrons moving towards the target core and it contains a tail with very high energy electrons (Figure 4-a).

4.2 Two-dimensional simulations

Within the work, two large scale simulations of laser plasma interaction in the two-dimensional geometry have been performed. Both simulations have been computed using a massively parallel relativistic electromagnetic PIC code EPOCH mentioned in the previous chapter. The laser beam parameters have been set according to the high-power iodine laser system PALS in Czech Academy of Sciences. More specifically, the parameters correspond to the attributes of laser beam at its fundamental wavelength, which is $\lambda = 1.315\,\mu$m. At this wavelength, the laser is capable to deliver energy of E = 1kJ. The intensity of laser light was $I = 1 \cdot 10^{20}\,\mathrm{W/m^2}$ for both simulations, thus the maximum laser dimensionless potential is $a_0 = 0.1123$. The beam profile is Gaussian in both, space and time, focused to the distance of $x = 50\,\mu$m from the entry boundary. The FWHM was equal to $10\,\mu$m and the pulse duration has been set to t = 20 ps. These parameters do not correspond to the laser PALS. The real parameters have been decreased because of our limited computational resources.

Initial parameters of plasma have been taken from the hydrodynamic simulations, which have been performed recently. The electron and ion densities were equal in both simulations, described by exponential profile with the scale length $L = 90\,\mu$m. The critical density is $n_c = 6.46 \cdot 10^{26}\ \mathrm{m^{-3}}$, which is the maximum density in both simulations. The simulations differ in chosen temperatures which are constant throughout the target. The first one has been performed with the electron temperature $T_e = 0.5$ keV and the temperature of ions $T_i = 0.5$ keV, while the second one has $T_e = 2.5$ keV and $T_i = 0.5$ keV.

To include the density profile up to the critical density, the simulation domain has the size of $381.35\,\mu\mathrm{m} \times 52.6\,\mu\mathrm{m}$. The size of individual cells has to be comparable to the minimum Debye length in the simulation box. However, in order to reduce the computational time, the size of the cells has been chosen a little bit larger, 50 nm × 50 nm, while the required accuracy of computations is still maintained. This corresponds to the number of cells in both directions 7540×1040, thus the total number of cells in simulations was approximately $8.3 \cdot 10^6$. The simulations are performed on the time scale of 20 ps, one simulation time step was approximately $\tau = 0.1$ fs to fulfill the CFL condition, thus the total number of time steps was about $2 \cdot 10^5$. Simulations contain two species of particles - electrons and ions. Both species have density 8 particles per cell, thus there is around $1.3 \cdot 10^8$ computational particles in total.

In both simulations, Convolutional Perfectly Matched Layer (CPML) boundary conditions have been used. On each boundaries, absorbing conditions were specified. The laser has been attached to the left boundary, and the beam is propagating along the x direction. The thickness of the CPML boundary conditions is 26 cells. For the simulation with $T_e = 0.5$keV, the special boundary condition to absorb the kinetic energy flux into the target, which is described in the beginning of this chapter, has been used.

The collisions of plasma particles are accounted for both simulations. Using formulas (2.6) and (2.32), one can theoretically estimate their effect. For the simulation with electron temperature $T_e = 0.5$ keV, the average time between two collisions evaluated at the critical

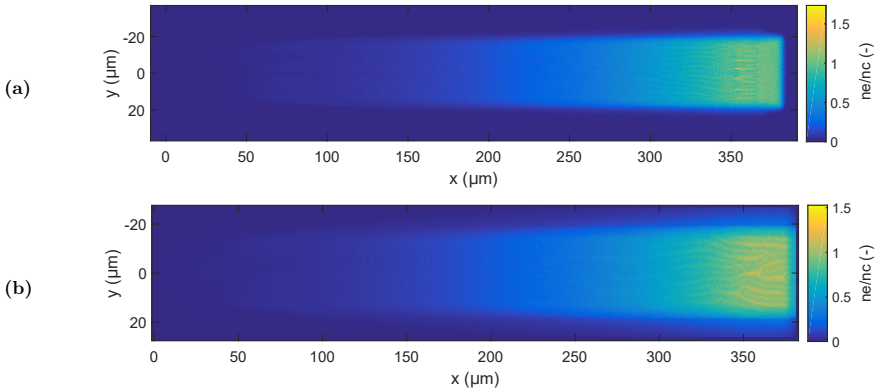

Figure 5: Electron density at the time 10 ps for the case of simulation with electron temperature 0.5 keV **(a)** and for the case of simulation with electron temperature 2.5 keV **(b)**. Figure shows cavities in the density profile and the continuous expansion of the plasma.

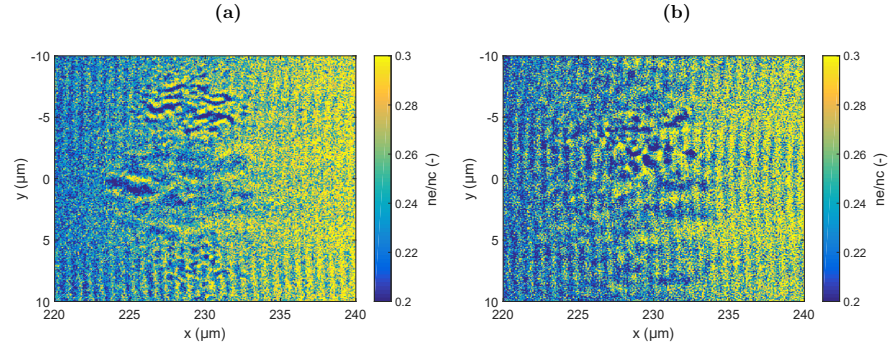

Figure 6: Cavities formed at quarter of critical density at the time 10 ps for the case of simulation with electron temperature 0.5 keV **(a)** and for the case of simulation with electron temperature 2.5 keV **(b)**. Density cavities contribute to the total absorption of the incident laser light. Electron plasma waves are also observed.

density is $1/\nu_{ei} = 1.1$ ps and the absorption coefficient calculated for the initial conditions is $\alpha_{abs} = 0.55$. For the simulation with electron temperature $T_e = 2.5$ keV, the average time between two collisions at the critical density is obviously higher, $1/\nu_{ei} = 8.2$ ps, thus the

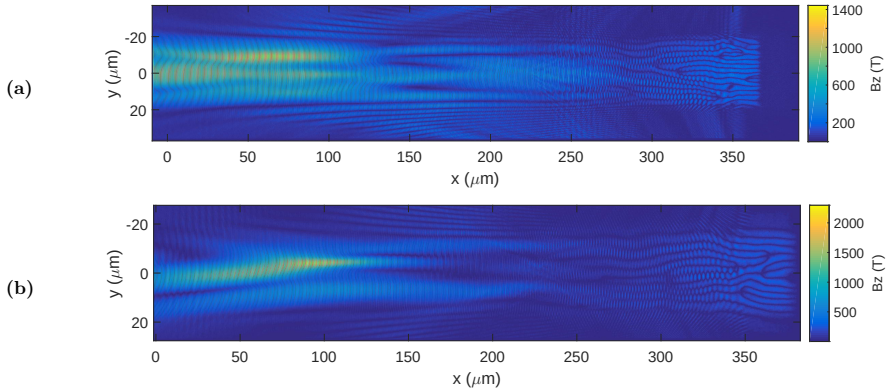

Figure 7: Z-component of the magnetic field at the time 10 ps for the case of simulation with electron temperature 0.5 keV **(a)** and for the case of simulation with electron temperature 2.5 keV **(b)**. Figure shows the filamentation of the incident beam.

absorption coefficient is only about $\alpha_{abs} = 0.09$. However, since the time scale of simulations is relatively long, the contribution of collisions to absorption cannot be neglected for both cases.

The threshold for the laser stimulated instabilities increases as the laser wavelength decreases. Thus one can expect, that the parametric instabilities might play important role, since wavelength of the incident laser light is relatively long. Scattered radiation on the frequency of incident laser beam corresponds to the reflection at the critical density and stimulated Brillouin scattering. The dependency of Brillouin scattering frequency on the plasma density is governed by following relation [15],

$$\omega = \omega_0 - 2k_0(c_s + u), \quad k_0 = \frac{\omega_0}{c}\sqrt{1 - \frac{n_e}{n_c}}, \tag{4.1}$$

where u is the velocity of expanding plasma. Thus the frequency shift of the stimulated Brillouin scattering is caused by ion acoustic wave and Doppler effect.

Radiation scattering takes place as well on the half of the frequency of the incident laser light, which corresponds to stimulated Raman scattering. The weak radiation might be also registered on the quarter of the fundamental frequency and can be interpreted as secondary Raman scattering of the reflected electromagnetic wave. Raman scattering is dependent on the instantaneous intensity of the incident electromagnetic wave and it can be described as a space localized instability, which is either absolute or convective. In the absolute case, the

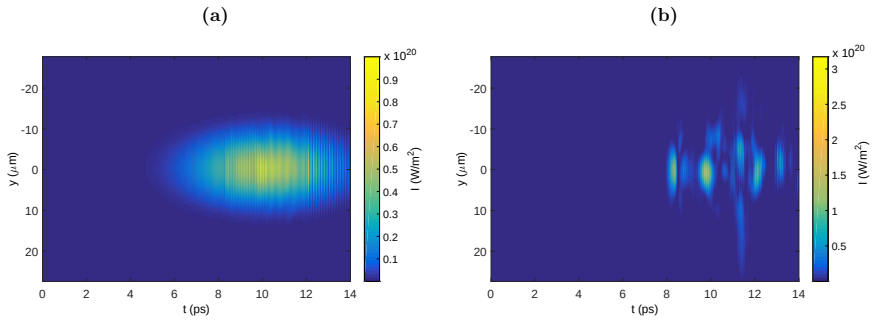

Figure 8: Intensity of the incident laser light **(a)** and scattered radiation **(b)** passing through the entry boundary for the case of simulation with electron temperature 0.5 keV.

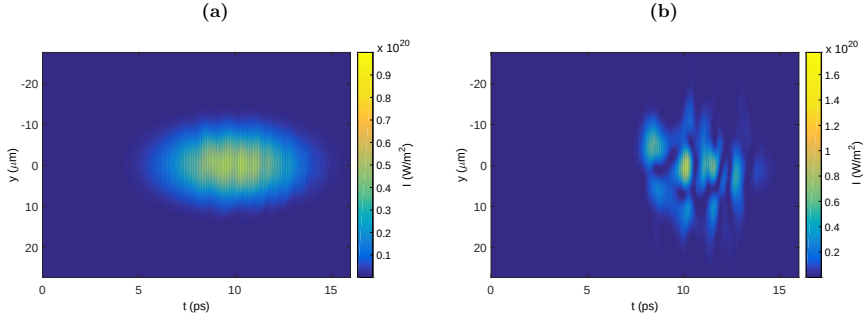

Figure 9: Intensity of the incident laser light **(a)** and scattered radiation **(b)** passing through the entry boundary for the case of simulation with electron temperature 2.5 keV.

temporal growth of the instability is localized while in the convective case the most unstable region is propagating with the laser wave. In the corresponding area, significant changes of the plasma parameters may occur.

The Figure 5 shows the electron density at the time 10 ps. Plasma is expanding much more in the case of simulation with $T_e = 2.5$keV (Figure 5-b), because the initial temperature is relatively high. Until the time 10 ps, plasma is continuously expanding, but the scale length of its profile remains unchanged during the whole simulation. After this moment, the intensity of the incident laser pulse reaches its maximum, thus the ponderomotive force weakens and the expansion is faster. As mentioned before, the density cavities are created

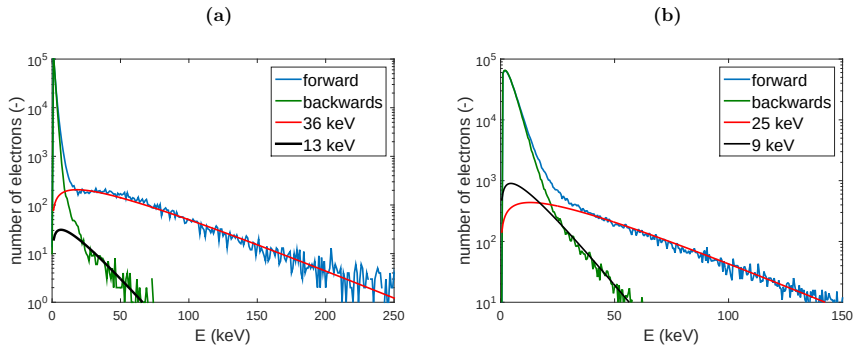

Figure 10: Distribution function of electrons going towards the target core and back in front of the implemented boundary condition for the case of simulation with electron temperature 0.5 keV **(a)** and for the case of simulation with electron temperature 2.5 keV **(b)**. Simulation data are approximated with Maxwellian distribution functions.

due to the Raman scattering on the quarter of the critical density. The cavities can be seen even better in Figure 6, which shows the electron density profile in the detail around quarter of the critical density. Emphasize, that this might not correspond to reality because the cavitation is three-dimensional phenomena [16]. The part of the electromagnetic field is caught in the cavities and cannot escape. Caught radiation is continuously converted into the kinetic energy of plasma. Thus this can also be one of the important absorption mechanisms of the incident laser light.

The total absorption of the incident laser energy in plasma for the simulation with $T_e = 0.5$keV has been 42.4 %, for the case of simulation with $T_e = 2.5$keV, the total absorption rate was significantly lower, about 33.1 %. According to the previous theoretical calculations, the Coulomb collisions between electrons and ions should have been the dominant mechanism of absorption in the first case, whilst in the second case, the major part of laser energy should have been absorbed by the density cavities, filamentation and parametric instabilities. These calculations, however, do not have to be accurate because they do not describe the interaction completely; there might be a wide range of other processes that lead to the absorption or scattering of the incident laser light. In order to distinguish the rate of absorption due to individual processes in plasma, further investigation of the simulation results has to be done.

Figure 7 shows the z-component of the magnetic field at the time 10 ps. Here, one can clearly observe the filamentation of the incident laser light behind x = 250 μm for both cases, which corresponds to the half of the critical density. In this region, the laser intensity is above the threshold for the relativistic self-focusing. Not only the incident but also the scattered wave is filamented.

Figures 8 and 9 show the flux of intensity of the incident laser beam and the scattered radiation through the entry boundary. The peak intensity of scattered radiation is almost three times higher than the intensity of the incident laser light for the case of the simulation with $T_e = 0.5\,\mathrm{keV}$. For the simulation with $T_e = 2.5\,\mathrm{keV}$, the laser beam intensity is increased in plasma approximately two times.

Energy spectrum of electrons propagating through the imaginary border in the place of the beginning of the boundary condition is plotted in Figure 10. According to the recent simulations [17], it seemed that the temperature of hot electrons does not depend on the intensity of the incident laser pulse and can be estimated in order of several tens of keV. In addition, recent studies showed, that these hot electrons themselves might drive a strong spherical convergent shock wave [27]. Thus the excessive preheat of the compressed fuel caused by these electrons in the late phase of compression would not have to be significant, since the major contribution to preheat of the core comes from electrons with energy higher than 100 keV which are able to penetrate the compressed shell and the amount of such electrons is relatively small. This fact could completely change the point of view on the parametric instabilities in the context of the shock ignited inertial fusion.

The favorable results have been confirmed in the presented simulations of laser system PALS. The temperature of the hot electrons propagating in forward direction into the target has been estimated to 36 keV for the case of simulation with electron temperature $T_e = 0.5\,\mathrm{keV}$ (Figure 10-a) and 25 keV for the case of simulation with $T_e = 2.5\,\mathrm{keV}$ (Figure 10-b). By integrating the corresponding Maxwellian functions, one can estimate how large are the fractions of hot electrons. In the first case, the fraction is about 0.024 % of all electrons in the simulation box. In the second case, the fraction is higher, about 0.037 %, which is consistent with previous theoretical absorption rate estimates and points out the presence of other non-linear absorption processes. Nevertheless, the number of hot electrons in both cases is relatively low; taking into account their energy, these electrons probably would not pass into the target core, which is in accordance with recent studies [27].

Finally, the temperature of electrons moving back into the interaction domain is in both simulations only a little bit higher than the initial temperature and does not contain any significant high energy tail. Therefore the boundary conditions behave in accordance with our requirements to suppress the return current of hot electrons. These and the previous results are also important for the interpretation of ongoing experiments in the laser facility PALS.

Conclusion

The work briefly presents the introduction to the inertial fusion research as well as basic physical processes which take place during the interaction of intense laser pulse with plasma. Particularly, for better interpretation and understanding of ongoing experiments that study the possibilities of nuclear fusion ignition by shock wave, the conditions of interaction have been set accordingly to them.

The main benefits of this work are successful implementation of boundary conditions for the effective absorption of hot electrons in the two-dimensional version of the computational code EPOCH. Its correct functionality has been later verified by plenty of numerical tests. Afterwards, two large scale simulations of laser system PALS in two-dimensional geometry on its fundamental wavelength 1,315 μm with intensity $1 \cdot 10^{20}\,\mathrm{W/m^2}$ and with initial electron temperatures $T_e = 0.5\,\mathrm{keV}$ and $T_e = 2.5\,\mathrm{keV}$ have been performed. Both simulations capture the time period of 20 ps. Simulations have been performed using the particle-in-cell code EPOCH [1]. Initial profiles of plasma density and temperature have been approximated from hydrodynamic simulations, which have been performed previously.

The total absorption of incident laser energy in plasma for the case of the simulation with $T_e = 0.5\,\mathrm{keV}$ was estimated to 42.4 %, for the case of the simulation with $T_e = 2.5\,\mathrm{keV}$, the total absorption was significantly lower, about 33.1 %. The temperature of the hot electrons in the case of the simulation with $T_e = 0.5\,\mathrm{keV}$ was estimated to 36 keV, in the case of the simulation with $T_e = 2.5\,\mathrm{keV}$ the temperature was about 25 keV. In both cases, the number of hot electrons is relatively low and their temperatures are not too high to prevent the fuel target compression in the later phase. However, it is necessary to further investigate their effect performing more accurate simulations.

Acknowledgments

I wish express my gratitude to my supervisor doc. Ing. Ondřej Klimo, Ph.D.for constant support and guidance, as well as for providing invaluable advice and direction.

Access to computing and storage facilities owned by parties and projects contributing to the National Grid Infrastructure MetaCentrum, provided under the programme "Projects of Large Infrastructure for Research, Development, and Innovations" (LM2010005), is greatly appreciated.

Access to the CERIT-SC computing and storage facilities provided under the programme Center CERIT Scientific Cloud, part of the Operational Program Research and Development for Innovations, reg. no. CZ. 1.05/3.2.00/08.0144, is greatly appreciated.

The development of the EPOCH code was funded in part by the UK EPSRC grants EP/G054950/1, EP/G056803/1, EP/G055165/1 and EP/ M022463/1.

Bc. Petr Valenta

Bibliography

[1] T D Arber, K Bennett, C S Brady, A Lawrence-Douglas, M G Ramsay, N J Sircombe, P Gillies, R G Evans, H Schmitz, A R Bell, and C P Ridgers. Contemporary particle-in-cell approach to laser-plasma modelling. *Plasma Physics and Controlled Fusion*, 57(11):113001, 2015.

[2] S. Atzeni and J. Meyer-ter-Vehn. *The Physics of Inertial Fusion: Beam Plasma Interaction, Hydrodynamics, Hot Dense Matter*. Oxford science publications. Clarendon Press, 2004.

[3] M M Basko. Physics and prospects of inertial confinement fusion. *Plasma Physics and Controlled Fusion*, 35(SB):B81, 1993.

[4] D. Batani, S. Baton, A. Casner, S. Depierreux, M. Hohenberger, O. Klimo, M. Koenig, C. Labaune, X. Ribeyre, C. Rousseaux, G. Schurtz, W. Theobald, and V.T. Tikhonchuk. Physics issues for shock ignition. *Nuclear Fusion*, 54(5):054009, 2014.

[5] R. Betti et al. Shock ignition: A new approach to high gain inertial confinement fusion on the national ignition facility. *Phys. Rev. Lett.*, 103(4), 2009.

[6] C. K. Birdsall and A. B. Langdon. *Plasma Physics via Computer Simulation*. Series in Plasma Physics. CRC Press, 2004.

[7] A.M. Bradshaw, T. Hamacher, and U. Fischer. Is nuclear fusion a sustainable energy form? *Fusion Engineering and Design*, 86(9–11):2770 – 2773, 2011. Proceedings of the 26th Symposium of Fusion Technology (SOFT-26).

[8] S. Eliezer. *The Interaction of High-Power Lasers with Plasmas*. Series in Plasma Physics. CRC Press, 2010.

[9] T. Zh. Esirkepov. Exact charge conservation scheme for particle-in-cell simulation with an arbitrary form-factor. *Computer Physics Communications*, 135(2), 2001.

[10] H. Fehske, R. Schneider, and A. Weiße. *Computational Many-Particle Physics*. Springer, 2008.

[11] Kai Germaschewski, William Fox, Narges Ahmadi, Liang Wang, Stephen Abbott, Hartmut Ruhl, and Amitava Bhattacharjee. The plasma simulation code: A modern particle-in-cell code with load-balancing and gpu support. *arXiv preprint arXiv:1310.7866*, 2013.

[12] H. Gould, J. Tobochnik, and W. Christian. *An introduction to computer simulation methods: applications to physical systems*. Addison–Wesley series in physics. Addison–Wesley, 3 edition, 2007.

[13] R. W. Hockney and J. W. Eastwood. *Computer Simulation Using Particles*. CRC Press, 2010.

[14] D. A. Jaroszynski, R. Bingham, and R. A. Cairns. *Laser-Plasma Interactions*. Scottish Graduate Series. CRC Press, 2009.

[15] O. Klimo et al. Particle-in-cell simulations of laser–plasma interaction for the shock ignition scenario. *Plasma Physics and Controlled Fusion*, 52(5), 2010.

[16] O Klimo, J Psikal, V T Tikhonchuk, and S Weber. Two-dimensional simulations of laser–plasma interaction and hot electron generation in the context of shock-ignition research. *Plasma Physics and Controlled Fusion*, 56(5):055010, 2014.

[17] O. Klimo and V. T. Tikhonchuk. Laser–plasma interaction studies in the context of shock ignition: the regime dominated by parametric instabilities. *Plasma Physics and Controlled Fusion*, 55(9), 2013.

[18] G. Lapenta. Particle in cell methods with application to simulations in space weather. Lecture notes.

[19] J D Lawson. Some criteria for a power producing thermonuclear reactor. *Proceedings of the Physical Society. Section B*, 70(1):6, 1957.

[20] R. Lichters, J. Meyer-ter-Vehn, and R. Pfund. *LPIC++: A Parallel One-dimensional Relativistic Electromagnetic Particle-In-Cell Code for Simulating Laser–Plasma–Interaction*. Max-Planck-Institut für Quantenoptik. MPQ, 1997.

[21] M. Murakami and J. Meyer ter Vehn. Indirectly driven targets for inertial confinement fusion. *Nuclear Fusion*, 31(7):1315, 1991.

[22] M. L. E. Oliphant and Lord Rutherford. Experiments on the transmutation of elements by protons. *Proceedings of the Royal Society of London A: Mathematical, Physical and Engineering Sciences*, 141(843):259–281, 1933.

[23] T. Pang. *An introduction to computational physics*. Cambridge University Press, 2 edition, 2006.

[24] S. Pfalzner. *An Introduction to Inertial Confinement Fusion*. Series in Plasma Physics. CRC Press, 2006.

[25] Ribeyre, X., Tikhonchuk, V.T., Breil, J., Lafon, M., Vallet, A., and Bel, E. Le. Analytical criterion for shock ignition of fusion reaction in hot spot. *EPJ Web of Conferences*, 59:03005, 2013.

[26] W. Theobald et al. Initial experiments on the shock-ignition inertial confinement fusion concept. *Physics of Plasmas*, 15(5), 2008.

[27] V T Tikhonchuk, A Colaïtis, A Vallet, E Llor Aisa, G Duchateau, Ph Nicolaï, and X Ribeyre. Physics of laser-plasma interaction for shock ignition of fusion reactions. *Plasma Physics and Controlled Fusion*, 58(1):014018, 2016.

[28] J. Villasenor and O. Buneman. Rigorous charge conservation for local electromagnetic field solvers. *Computer Physics Communications*, 69(2-3), 1992.

[29] K. Yee. Numerical solution of inital boundary value problems involving maxwell's equations in isotropic media. *IEEE Transactions on Antennas and Propagation*, 14(3), 1966.